Electronic Supplementary Information

High-strength, low infrared-emission nonmetallic films for highly efficient Joule/solar heating, electromagnetic interference shielding and thermal camouflage

Yuxuan Zhang[#], Lei Li[#], Yanxia Cao, Yanyu Yang, Wanjie Wang, Jianfeng Wang**

College of Materials Science and Engineering, Henan Key Laboratory of Advanced Nylon Materials and Application, Zhengzhou University, Zhengzhou 450001, China

[#] *Y. X. Zhang and L. Li contribute equally to this work.*

Electronic Supplementary Information Includes:

1: Experimental Procedures;

2: Fig. S1～Fig. S44;

3: Table. S1～Table. S5.

Experimental Procedures

* To whom correspondence should be addresses. (Prof. Wang, Email: wwj@zzu.edu.cn)
* To whom correspondence should be addresses. (Prof. Wang, Email: jfw@zzu.edu.cn)

Materials: Lithium fluoride (LiF) and hydrochloric acid (HCl) were provided by Shanghai Macklin Biochemical Co., Ltd., and Luoyang chemical reagent factory, respectively. Beijing Dk Nano technology Co. Ltd. provided Ti_3AlC_2 powders (98%-purity, 200-mesh). Nanjing XFNANO Materials Tech Co., Ltd. provided high purity flake graphite.

Preparation of $Ti_3C_2T_x$ MXene: In a Teflon beaker, 10 g LiF was dissolved into 200 mL 9 M HCl with subsequently stirring for 30 mins. Then, 10 g Ti_3AlC_2 powders were tardily added into the LiF/HCl mixture solution with subsequently stirring at 35 °C for 24 h. The resultant mixture was then continually rinsed with deionized (DI) water and centrifugation (3500 rpm) until the mixture pH was approximate to 6. Finally, the DI water was added to the resulting slurry, and the homogenous $Ti_3C_2T_x$ supernatant was collected by centrifuging at 3500 rpm after manual shaking for 10 mins.

Fabrication of MXene/GO multilayered film: GO nanosheets were fabricated according to an improved Hummer's method using graphitic powders. MXene/GO multilayered films were fabricated by vacuum-assisted alternating filtration approach. The MXene layer was designed as the surface layer of the multilayered film to display its low IR emissivity and high electrical conductivity, thus resulting n+1 number of MXene layers and n number of GO layers in the alternating multilayered films. Before filtration, the concentrations of both MXene dispersion

and GO dispersion were diluted to 1 mg/ml, the added MXene dispersion and GO dispersion were controlled to 12.5 ml in volume, and then evenly divided into n+1 and n equal parts. After that, the individual MXene dispersions and GO dispersions were filtered alternately through a filter membrane with the bottom and top layer being MXene. Finally, the multilayered films were dried at room temperature and peeled off from the filter membrane. The as-obtained MXene/GO multilayered films were named as MGM-(2n+1), where n+1 and n represent the number of MXene layers and GO layers in the multilayered film, respectively. For comparison, MXene/GO composite (MGC) film was prepared by solution blending filtration, in which the volume of MXene dispersion and GO dispersion was consistent with that of alternating filtration.

Characterization: The morphologies of MXene, GO, MGC, and MGM films were observed by TEM (G2F20 S-TWIN-TEM, Tecnai, 200 kV) and SEM (JSM-5900LV-SEM, 5 kV). MGM and MGC films were cut by focused ion beam (FIB) to provide cross-section using a FEI Helios NanoLab 600i. The surface chemistry was determined by FTIR (Vertex-70, Bruker) and XPS (Axis Supra, Kratos Analytical) spectra. Raman spectra was recorded using a Reflex Raman System (LabRAM HR Evolution, HORIBA Scientific, France) with a laser wavelength of 532 nm. Low-field nuclear magnetic resonance (LF-NMR, VTMR20-010V-1, Suzhou Niumag Co., Ltd., China) and Temperature-dependent FTIR (MAGNA-IR 560, Nicolet, USA) was performed to analyze hydrogen bonding interactions. XRD patterns were analyzed using a DX-

2700BH X-ray Diffractometer with Cu Ka radiation. The orientation degree was calculated by WAXS (D8 Discover, Bruker), using an incident Cu-Kα X-ray beam parallel to the film plane. The sample is 13.06 cm away from the detector. The WAXS samples were 1 mm wide, 10 mm long strips. The Herman's orientation factor (*f*), which is defined as follows, was used to determine the alignment degree of nanosheets[32],

$$f = \frac{1}{2}\left(3\langle \cos^2 \emptyset \rangle - 1\right) \quad (1)$$

where $\langle \cos^2 \emptyset \rangle$ is the average value of the square of the azimuthal angle's cosine for observed films, which is determined as follows,

$$\langle \cos^2 \emptyset \rangle = \frac{\int_0^{\pi/2} I(\emptyset)\cos^2 \emptyset \sin \emptyset d\emptyset}{\int_0^{\pi/2} I(\emptyset)\sin \emptyset d\emptyset} \quad (2)$$

where $I(\emptyset)$ is the intensity at an azimuthal angle of ϕ.

The IR reflectivity (ρ) and transmissivity (τ) were measured using a FTIR spectrometer (Nicolet iS50, Thermo Fisher) accompanied with an IR integrating sphere. The IR emissivity (ε) was then calculated according to the following equation: $\varepsilon = 1 - \rho - \tau$. Reflectivity ($\rho$) and transmissivity ($\tau$) in solar spectrum were measured using a UV−vis−NIR spectrometer (Lambda 1050+, PerkinELmer) accompanied with an integrating sphere attachment, and the UV−vis−NIR absorptivity (α) was calculated by the following equation: $\alpha = 1 - \rho - \tau$. Tensile stress-strain curves were recorded at a loading rate of 0.5 mm/min (using a SAAS EUT4104 Tester with a 500 N load cell) under 30% humidity and a temperature of 25 °C. To ensure the sample does not damage when fixed to the testing apparatus, the sample was adhesively

attached to a paper frame with a rectangular hole large enough to fit the gauge length (10 mm) and sample width (2 mm). The averaged mechanical properties and corresponding standard deviations for each sample were obtained based on ten measurement results, where the few sample strips that broke near the clamps were excluded from the calculations. Macro-tribological test was performed according to standard ASTM G99-04 using a UMT-2MT tribometer (CETR) in a ball-on-plate contact configuration under 2 Hz and 2 N applied loads. Commercially available steel balls (φ = 3 mm, announced mean roughness = 0.02 μm) were used as the stationary upper counterparts, whereas the lower tested films were mounted onto the flat base and driven to slide reciprocally at distance of 0.5 cm. The friction coefficient-versus-time curves were recorded automatically. Nanoindentation test was performed according to standard ASTM E 2546 using Hysitron TI 980 (Hysitron, Bruker, USA) with a conical diamond indenter tip to study the surface hardness of the films. The curvature radius of the indenter tip was 5 μm and the cone angle was 90°. The electrical conductivity was tested through a standard four-probe technique (RTS-8). The thermal radiation temperature of different films was monitored by an IR thermograph (FLIR E75) in the indoor environment with an ambient temperature around 17 °C. Solar heating tests were performed outdoors at Zhengzhou University, China (east longitude: 113°32′; northern latitude: 34°48′). The actual temperature of 3×3 cm^2 films was determined using K-type thermocouples (DT1310 LIUHUAJIN) affixed to the shaded surface of the film in outdoor sunlight. For the outdoor solar heating test, a solar power meter (TES1333R) and a digital anemometer (PM6252B,

PEAKMETER) were utilized to real-time monitor the weather parameters. Joule heating performance was explored using a DC power (MS-3050D, MAISHENG). A constant DC voltage was applied to both ends of a 2×1 cm^2 film and the thermal radiation and actual temperature of the film was recorded using IR thermography. EMI shielding performance in the X-band was investigated by a vector network analyzer (Aglilent N5230) and a coaxial test cell (APC-7 connector) using round samples with a diameter of 12 mm. The scattering parameters (S_{11} and S_{21}) were studied to obtain SE_T, SE_R and SE_A according to the following equation:

$$R = |S_{11}|^2 \quad (3)$$

$$T = |S_{21}|^2 \quad (4)$$

$$SE_R = -\log_{10}(1 - R) \quad (5)$$

$$SE_A = -\log_{10}\left(\frac{T}{1 - R}\right) \quad (6)$$

$$SE_T = SE_A + SE_R \quad (7)$$

In addition, specific EMI SE considering thickness (SE_t) was obtained by dividing thickness as following equation (8), and specific EMI SE considering thickness and density (SSE_t) was obtained by dividing thickness and density as following equation (9):

$$SE_t = SE/t = dBcm^{-1} \quad (8)$$

$$SSE_t = SSE/t = dBcm^3g^{-1}cm^{-1} = dBcm^2g^{-1} \quad (9)$$

Calculation of thermal energy conversion efficiency: The energy input to film is defined as H_{in}, the energy loses to the ambient is defined as H_{loss}, and the thermal conversion efficiency is defined as η, particularly:

The solar-to-thermal conversion efficiency is calculated by

$$\eta = \frac{H_{in} - H_{loss}}{H_{in}} = \alpha - \frac{\varepsilon\sigma(T^4 - T_a^4)}{I_{solar}} \quad (10)$$

where α is the solar absorptivity, ε is the IR emissivity, T and T_a are the temperature of film and ambient, respectively, σ is the Stefan–Boltzmann constant (5.67032×10^{-8} W/(m^2·K^4)), I_{solar} is the solar irradiance in solar to thermal conversion test.

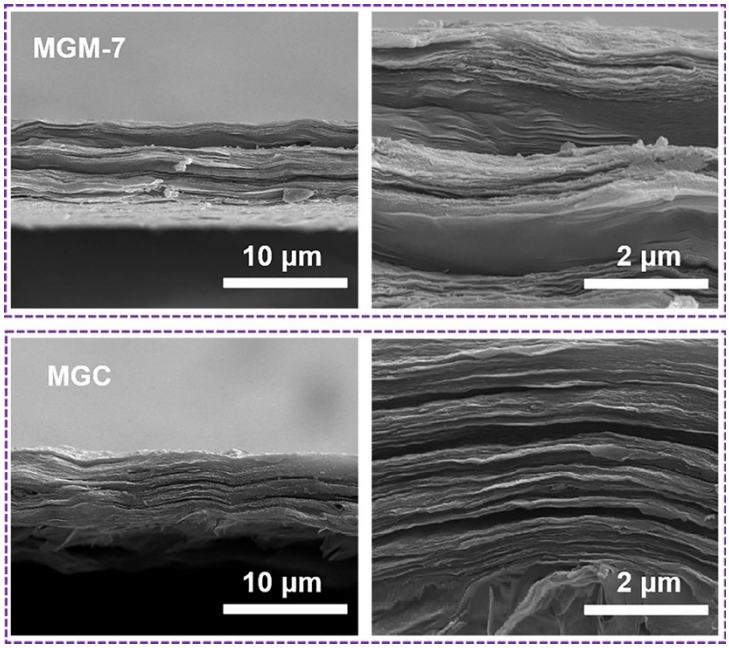

Fig. S1 Cross-sectional SEM images of MGM-7 and MGC films at different magnifications.

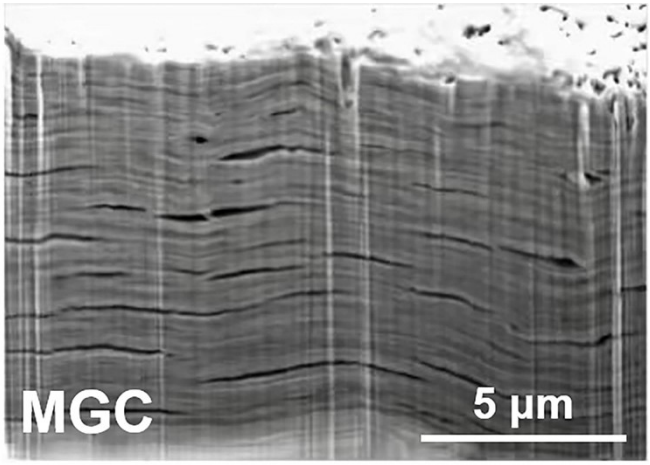

Fig. S2 SEM images of cross-section of MGC film cut by focused ion beam (FIB).

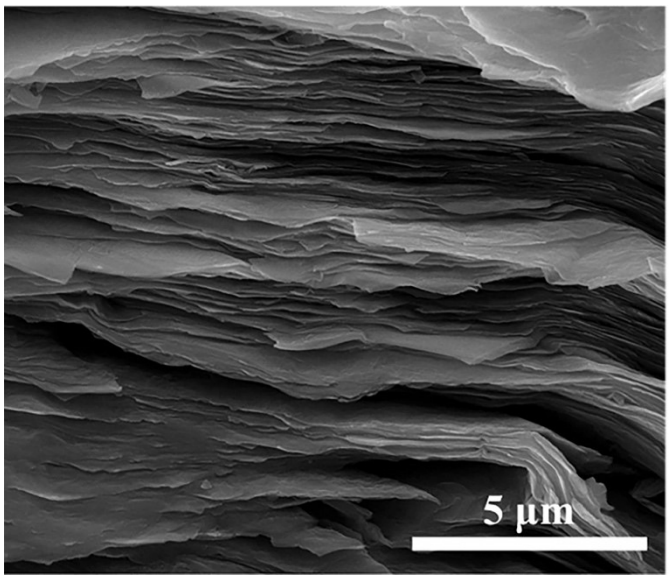

Fig. S3 Cross-sectional SEM image of pure MXene film.

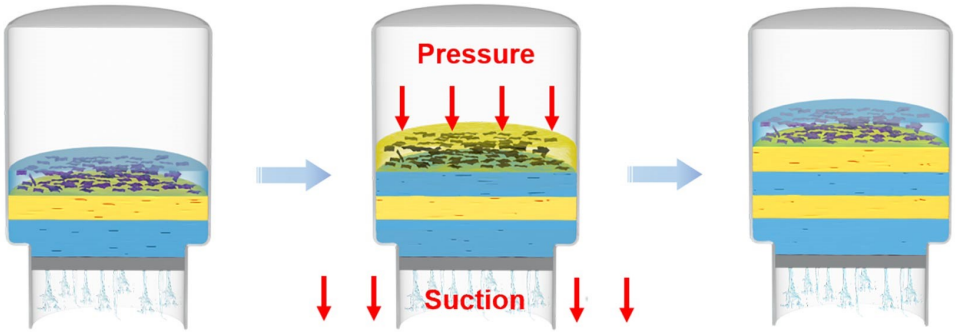

Fig. S4 Schematic illustration of fabrication process of MGM film by vacuum assisted alternating filtration method.

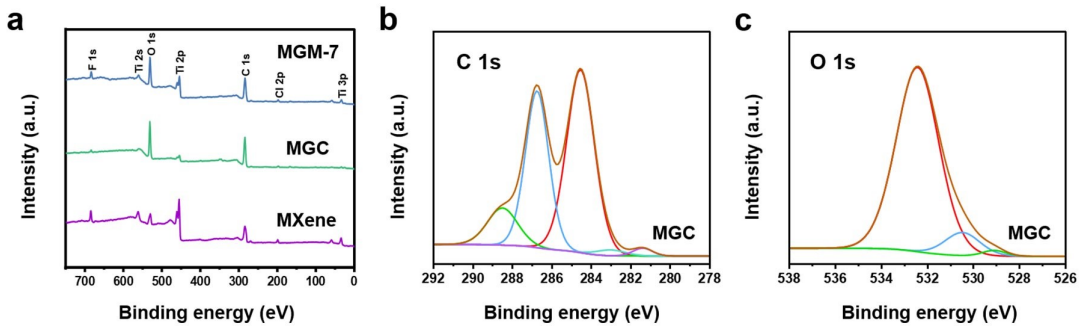

Fig. S5 (a) XPS wide-scan spectra of MXene, MGC, and MGM-7 films. High-resolution XPS spectra of MGC films of (b) C 1s and (c) O 1s.

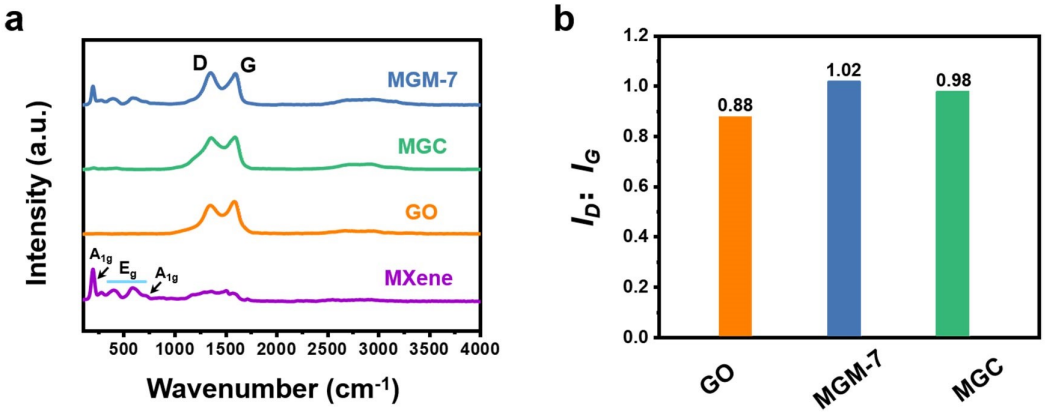

Fig. S6 (a) Raman spectra and (b) I_D/I_G ratio of MXene, GO, MGC, and MGM-7 films.

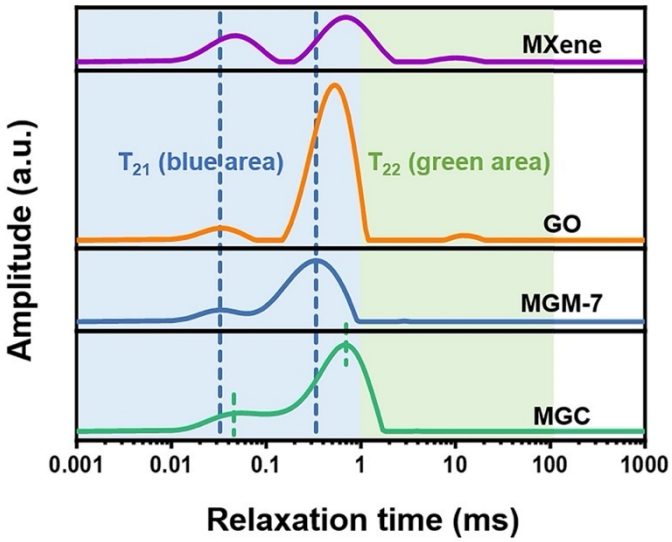

Fig. S7 Low-field NMR spectra of MXene, GO, MGC, and MGM-7 films.

The transverse relaxation time T_2 was divided into two parts, T_{21} (0-1 ms) and T_{22} (1-100 ms), where T_{21} represents the bound water capable of forming hydrogen bond with nanosheets inside the film. It can be intuitively noticed that the T_2 relaxation inversion spectra of MXene and GO films overlap after mixing. This phenomenon illustrates the interaction among MXene nanosheets and GO nanosheets in MGC and MGM-7 films. Notably, the relaxation time of T_{21} of MGM-7 film was significantly shorter than that of MGC, MXene, and GO films, verifying the formation of stronger hydrogen bonding interaction in MGM-7 film.

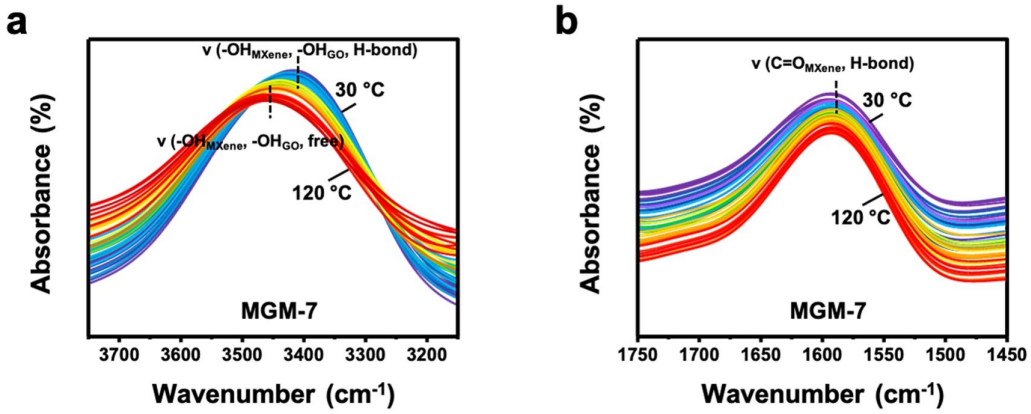

Fig. S8 Temperature-dependent FTIR spectra of MGM-7 film upon heating from 30 to 120 ℃ under the region of (a) 3750-3150 cm^{-1} and (b) 1750-1450 cm^{-1}.

Hydrogen bonding interactions show a temperature dependence and are always disrupted as the temperature increases, leading to a blue shift in the stretching vibrations of -OH and C=O. The stretching vibration band of hydroxyl group near 3392 cm^{-1} of MGM-7 film shifted to a high wavenumber (3468 cm^{-1}) with a gradual decrease in intensity when heated from 30 to 120 ℃ gradually. Meanwhile, the C=O stretching vibration spectral band near 1624 cm^{-1} also blue shifted upon heating. This shift indicates the transition of hydrogen bonds from combined state to dissociative state, revealing the breakage of hydrogen bonding groups and the gradual weakening of hydrogen bonding interactions during heating process. These results confirm the existence of multiple hydrogen bonding at molecular scale in MGM-7 film among MXene nanosheets in MXene layer, among GO nanosheets in GO layer, and between MXene and GO nanosheets at the interface of MXene layer and GO layer.

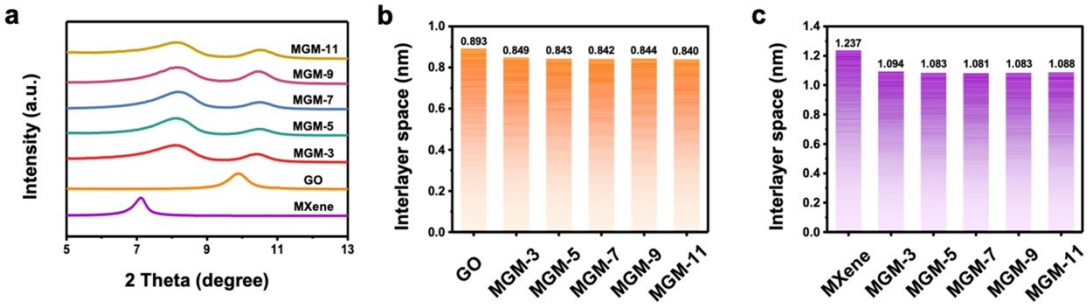

Fig. S9 (a) XRD patterns of MXene, GO, and MGM films. (b) Calculated interplanar spacing of GO nanosheets in different MGM films. (c) Calculated interplanar spacing of MXene nanosheets in different MGM films.

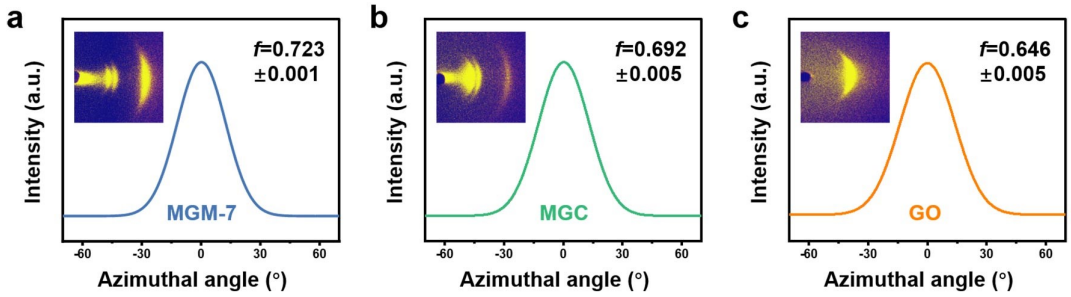

Fig. S10 WAXS patterns for an incident Cu-Kα X-ray beam parallel to the film plane and corresponding azimuthal scan profiles for the 001 peak for (a) MGM-7, (b) MGC, and (c) GO films.

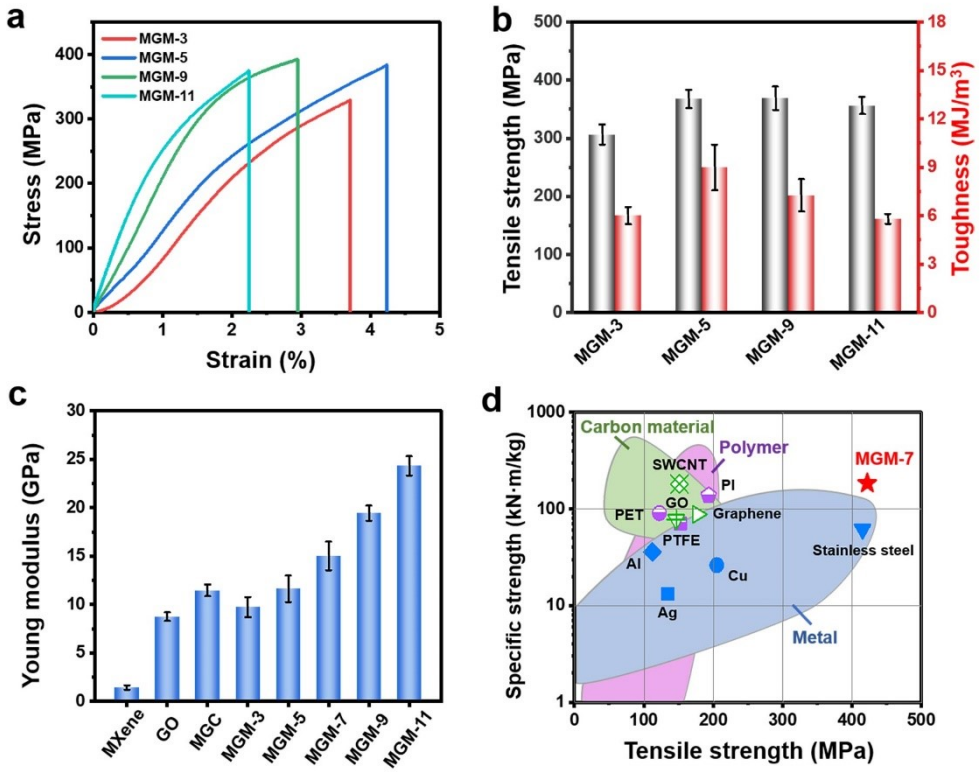

Fig. S11 (a) Tensile stress-strain curves, (b) tensile strength and fracture toughness of different MGM films. (c) Tensile Young's modulus of MXene, GO, MGC, and MGM films. (d) Comparison of specific strength of different types of materials.

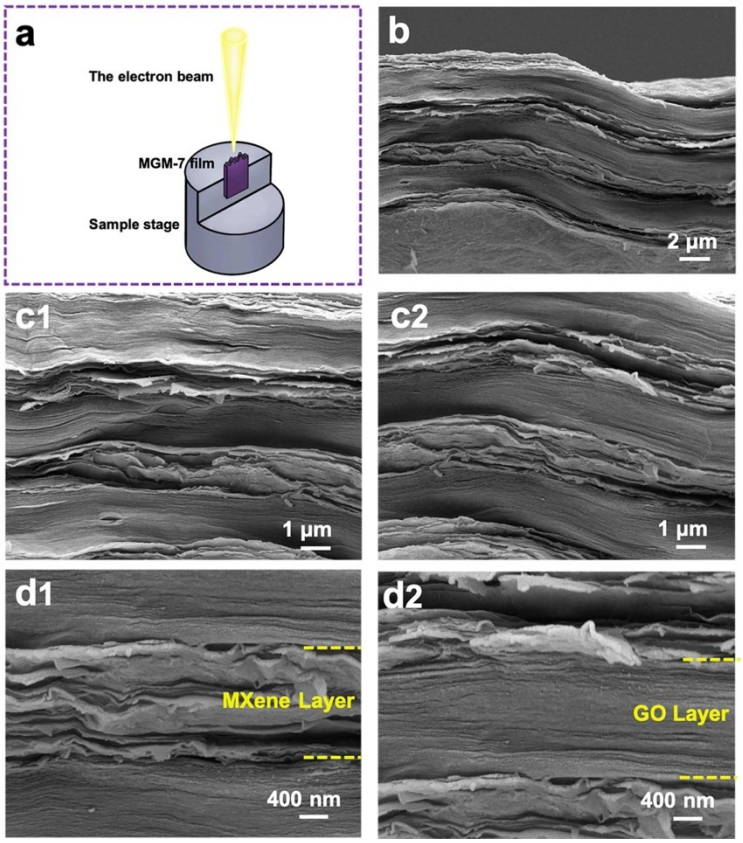

Fig. S12 SEM images of fracture surface of MGM-7 film at different magnifications observed from the direction perpendicular to fracture surface.

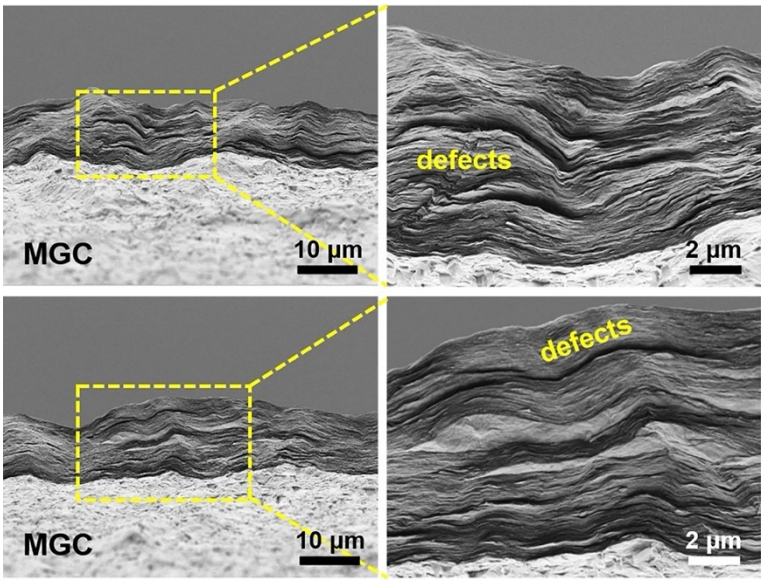

Fig. S13 SEM images of fracture surface of MGC film at different magnifications observed from the direction perpendicular to fracture surface.

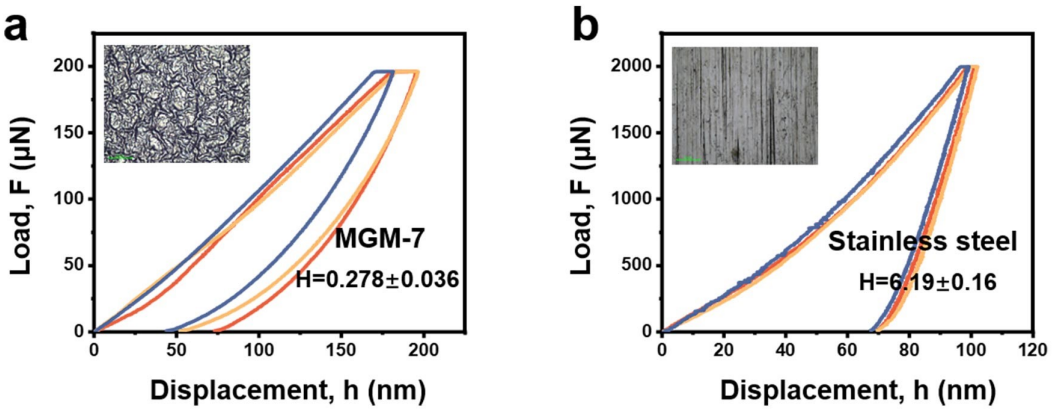

Fig. S14 Load-depth curve of nanoindentation for (a) MGM-7 and (b) Stainless steel films. Inset is their surface hardness value, respectively. As demonstrated, stainless steel film has a much higher hardness than MGM-7 film. This will limit the application of MGM film to some extent, whereas this does not negate the advantage of MGM film as well as its versatile application.

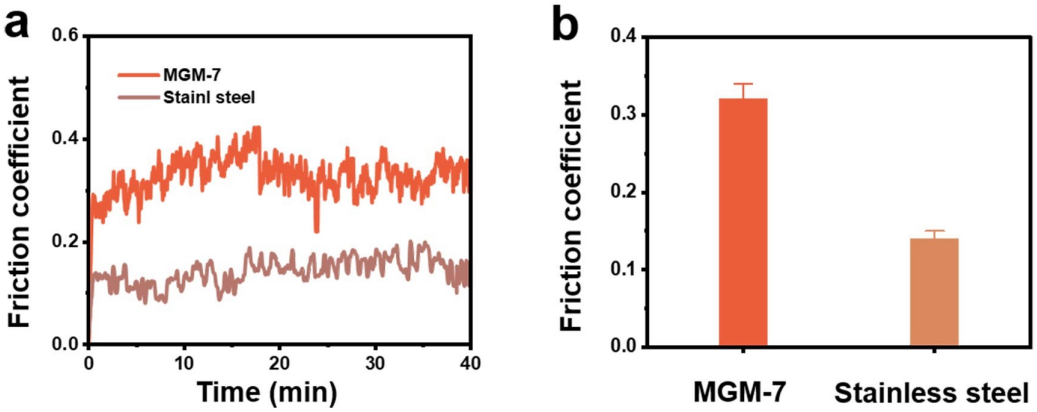

Fig. S15 (a) Variation in friction coefficient with time, (b) average friction coefficients of MGM-7 and stainless steel films. As shown in the above figures, MGM film has relatively excellent macroscopic friction resistance even though it is not superior to stainless steel film in term of macroscopic tribological properties.

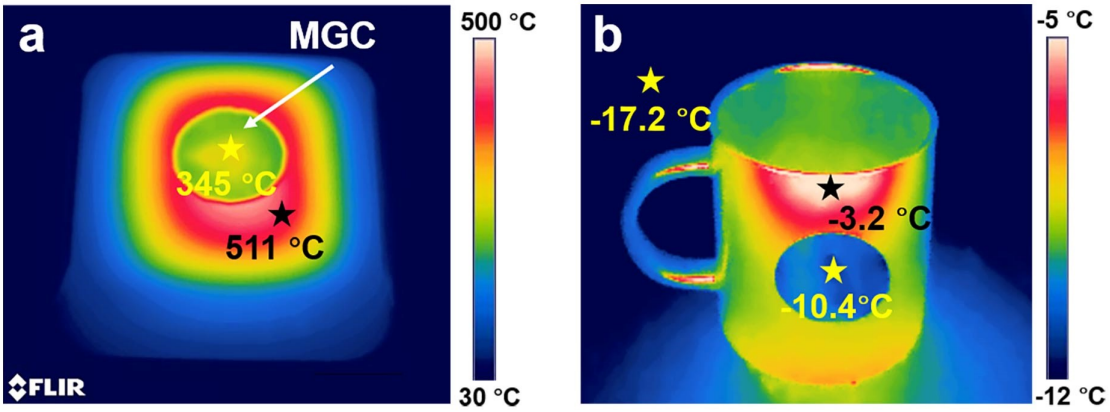

Fig. S16 (a) IR images of MGC film covering on an object with a thermal radiation temperature of 511 °C. (b) Thermal camouflage performance of MGC film covering on a cold ceramic cup.

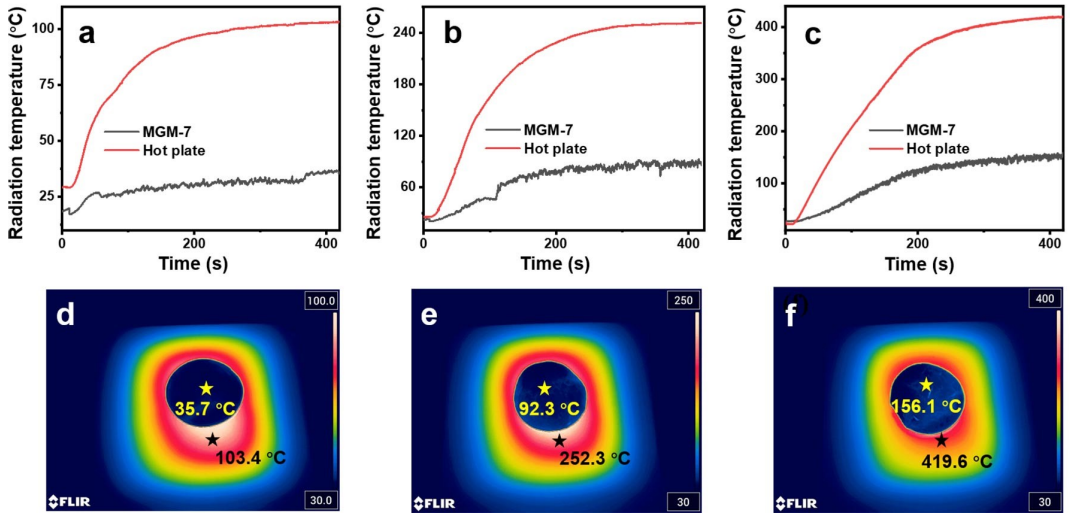

Fig. S17 (a-c) Measured indoor radiation temperature of MGM-7 film covering on an object with increasing temperatures. (d-f) IR images of MGM-7 film covering on the object with different temperatures. For an object with radiation temperature of 103.4, 252.3, and 419.6 ℃, the radiation temperature of MGM-7 films covering on the object was 35.7, 92.3, and 156.1 ℃, respectively, which was 67.7, 160, and 263.5 ℃ lower than that of the object.

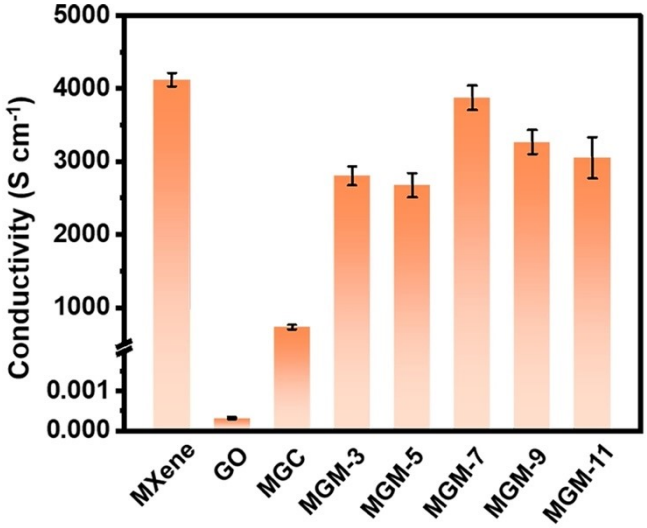

Fig. S18 Electrical conductivity of MXene, GO, MGC, and MGM films.

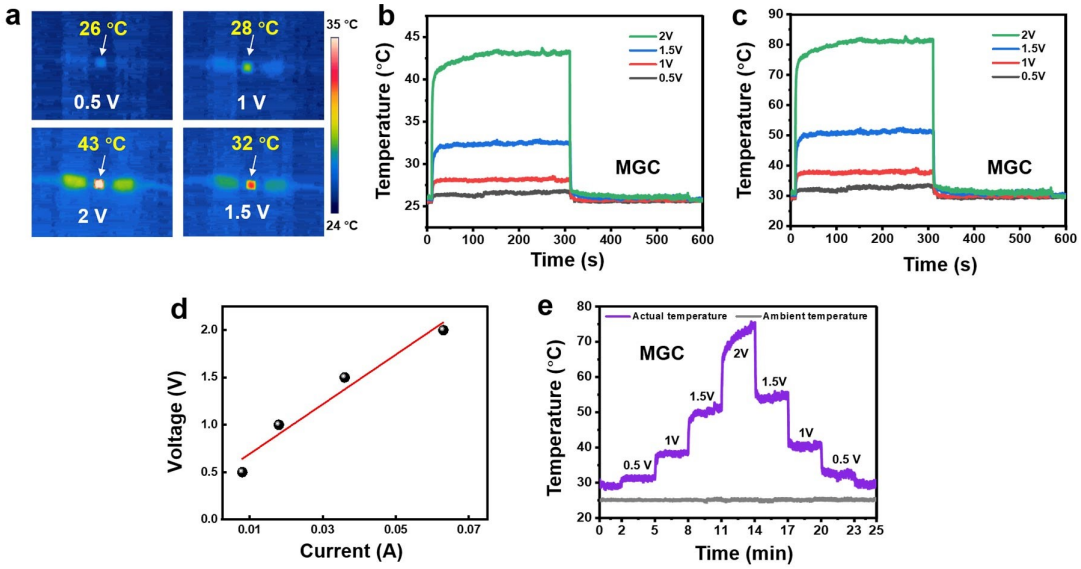

Fig. S19 Energy-saving heating performance of MGC film. (a) IR images, (b) IR thermal camouflage temperature and (c) actual temperature of MGC film at different driving voltages. (d) *I–V* curve of MGC film at different voltages. (e) Apparent and actual temperature of MGC film by adjusting the driving voltage from 0.5 to 2 V and from 2 to 0.5 V.

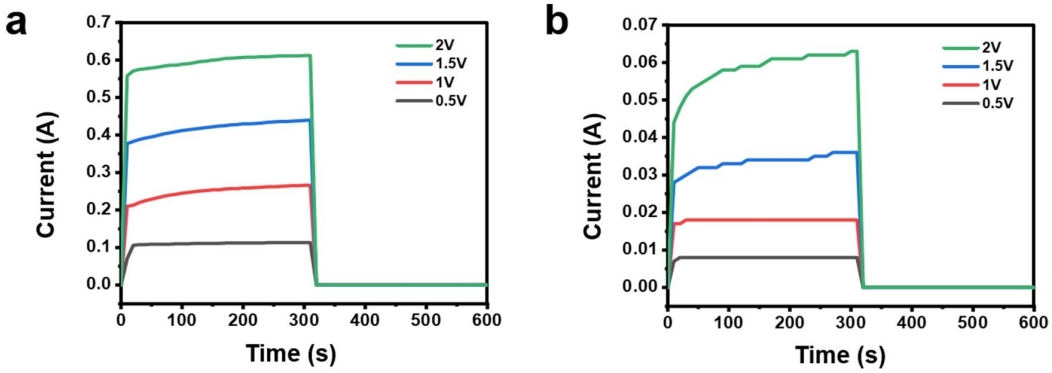

Fig. S20 Current changes in (a) MGM-7 film and (b) MGC film after applying different voltages.

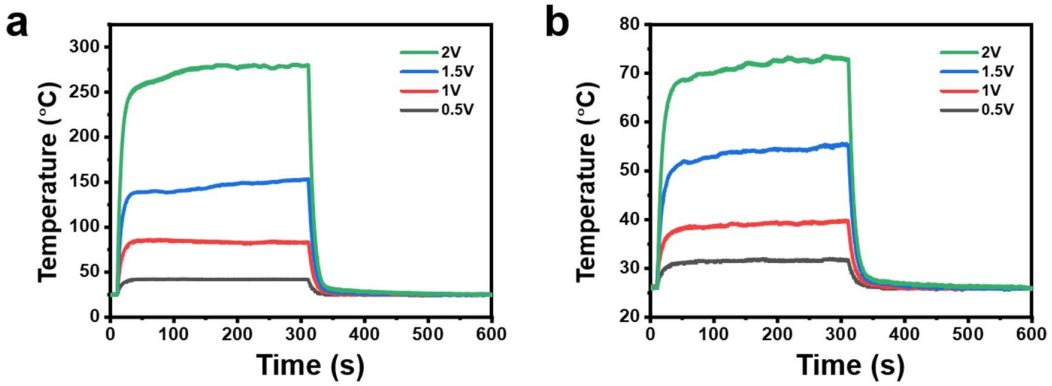

Fig. S21 The temperature of black insulated rubber tape covering onto (a) MGM-7 film and (b) MGC film after applying different driving voltages. The measured temperature of the insulating tape on MGM-7 film at 0.5, 1, 1.5, and 2 V was 48.2, 88.4, 151.7, and 278.5 °C, respectively, which was much higher than their thermal camouflage heating temperature but lower than their actual temperature measured by adjusting the emissivity of IR camera directly. This is because that the insulating tape increases the resistance of MGM-7 film, reducing the current flowing through MGM-7 film, and thus reducing its saturated Joule heating temperature.

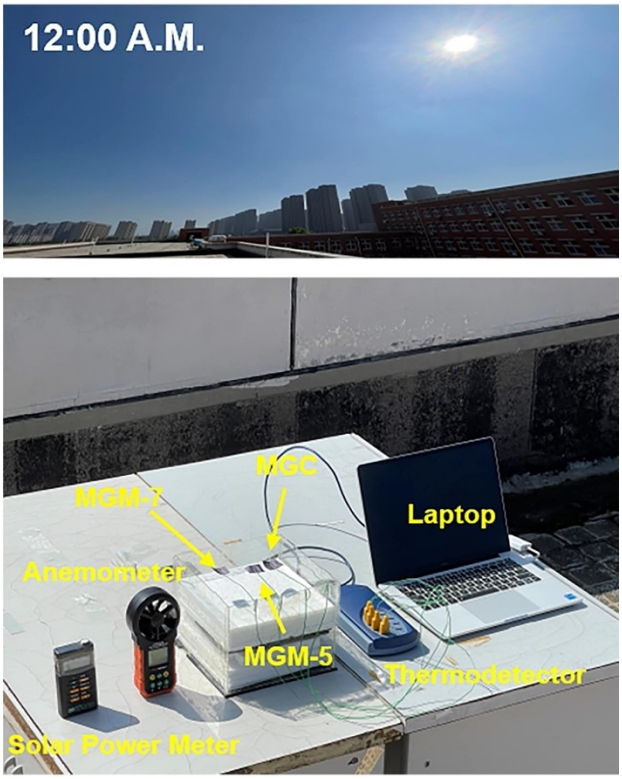

Fig. S22 Digital images of solar heating device in an outdoor environment on a sunny day (September 20, 2021, east longitude: 113°32′; northern latitude: 34°48′).

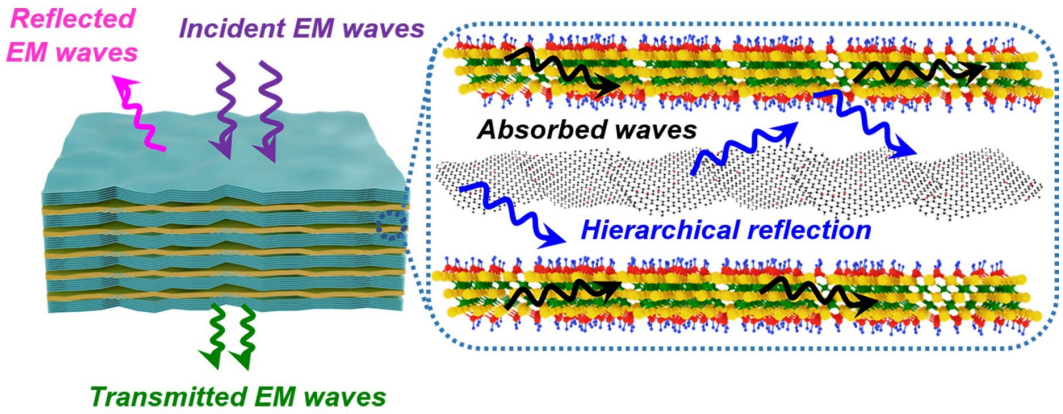

Fig. S23 Dissipation schematic of electromagnetic wave in MGM film.

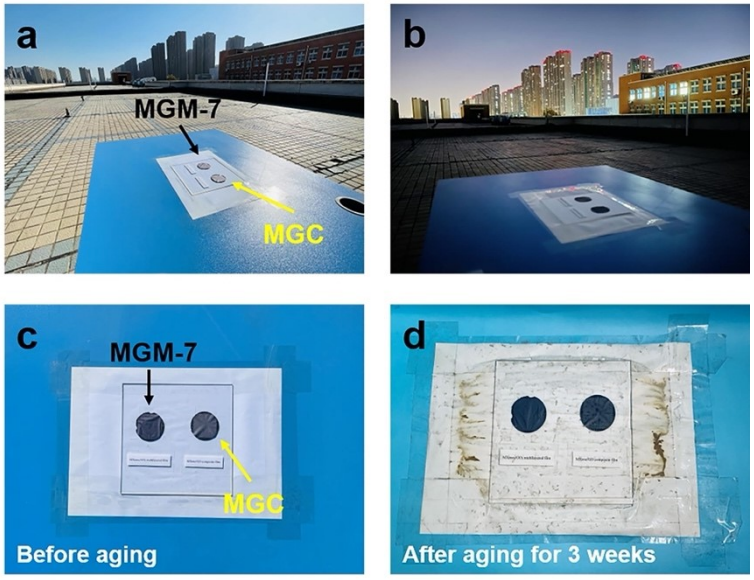

Fig. S24 Digital images of stability test placed outdoors for 3 weeks. (a) and (b) are digital images at daytime and night during outdoor aging test. (c) is the MGM-7 film and MGC film before outdoor aging test. (d) is the MGM-7 film and MGC film after outdoor aging test.

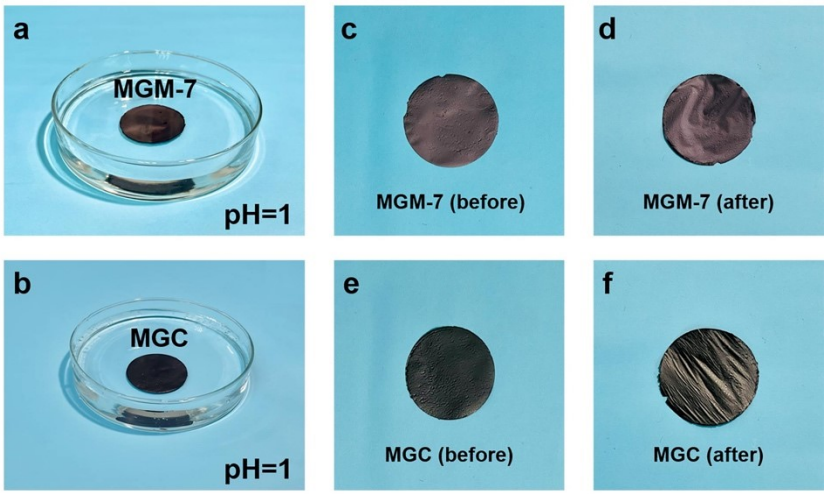

Fig. S25 Digital images of stability test in strong acid for two hours. (a) MGM-7 film and (b) MGC film immersed in strong acid. (c) and (d) are the MGM-7 film before and after being immersed in strong acid, respectively. (e) and (f) are the MGC film before and after being immersed in strong acid, respectively.

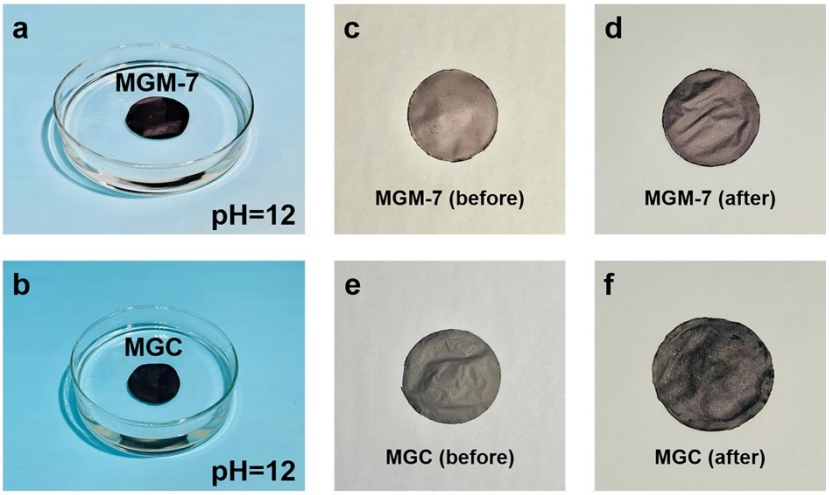

Fig. S26 Digital images of stability test in strong alkali for two hours. (a) MGM-7 film and (b) MGC film immersed in strong alkali. (c) and (d) are the MGM-7 film before and after being immersed in strong alkali, respectively. (e) and (f) are the MGC film before and after being immersed in strong alkali, respectively.

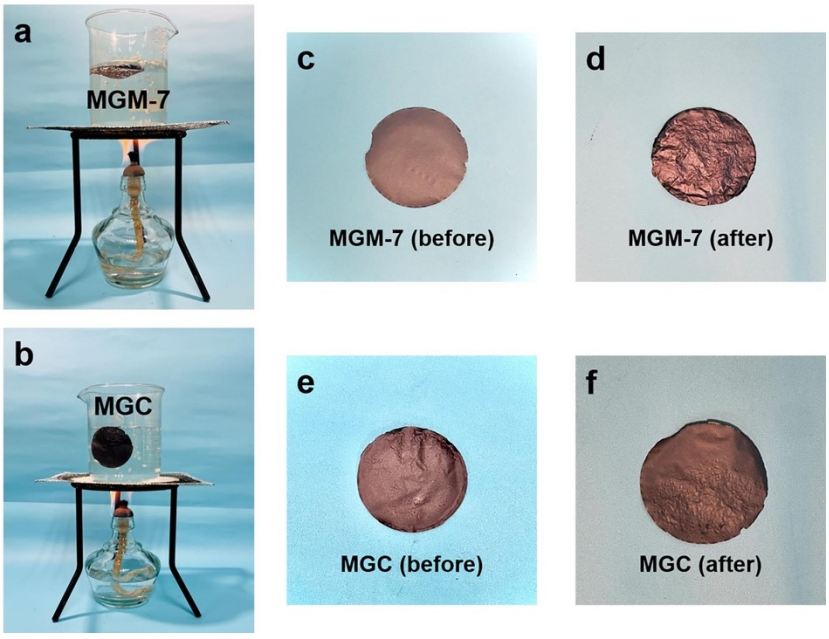

Fig. S27 Digital images of stability test immersed in boiling water for 5 mins. (a) MGM-7 film and (b) MGC film immersed in boiling water. (c) and (d) are the MGM-7 film before and after being immersed in boiling water, respectively. (e) and (f) are the MGC film before and after being immersed in boiling water, respectively.

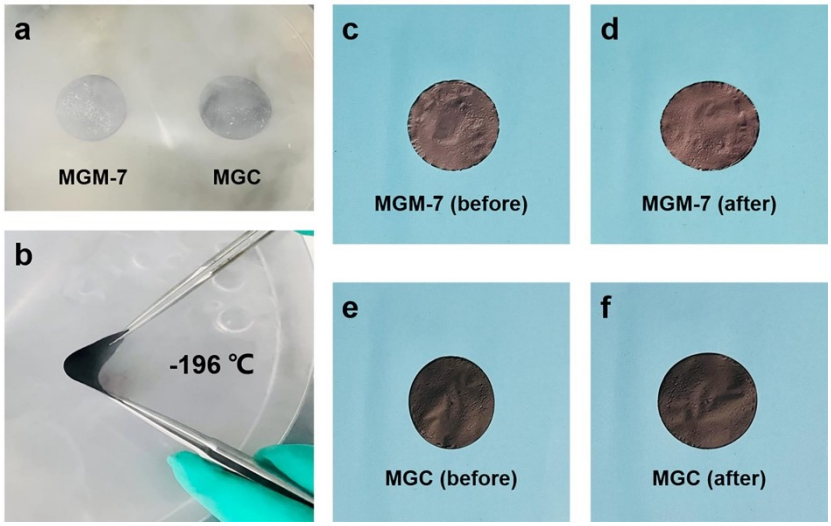

Fig. S28 Digital images of stability test in a cryogenic temperature environment of −196 °C in liquid N_2 for 10 mins. (a) MGM-7 film and MGC film placed in the liquid N_2. (b) Bended MGM-7 film in the liquid N_2. (c) and (d) are the MGM-7 film before and after cryogenic-temperature aging, respectively. (e) and (f) are the MGC film before and after cryogenic-temperature aging, respectively.

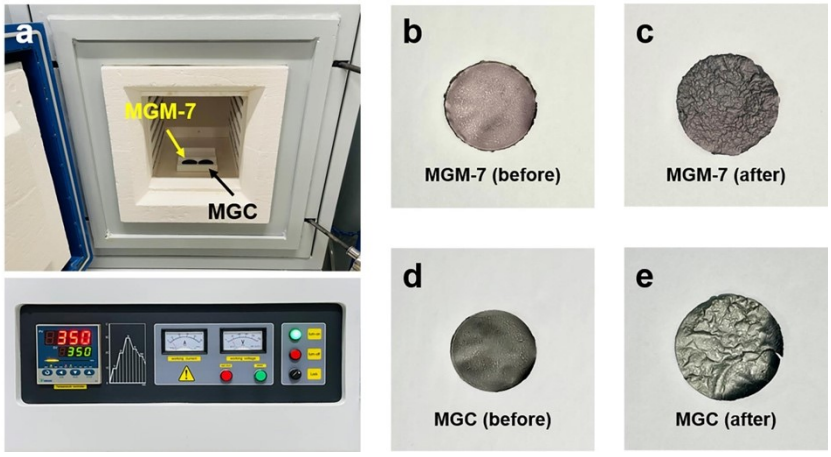

Fig. S29 Digital images of stability test in a high temperature aerobic environment (350 °C) for two hours. (a) MGM-7 film and MGC film placed in the muffle furnace. (b) and (c) are the MGM-7 film before and after high-temperature aging, respectively. (d) and (e) are the MGC film before and after high-temperature aging, respectively.

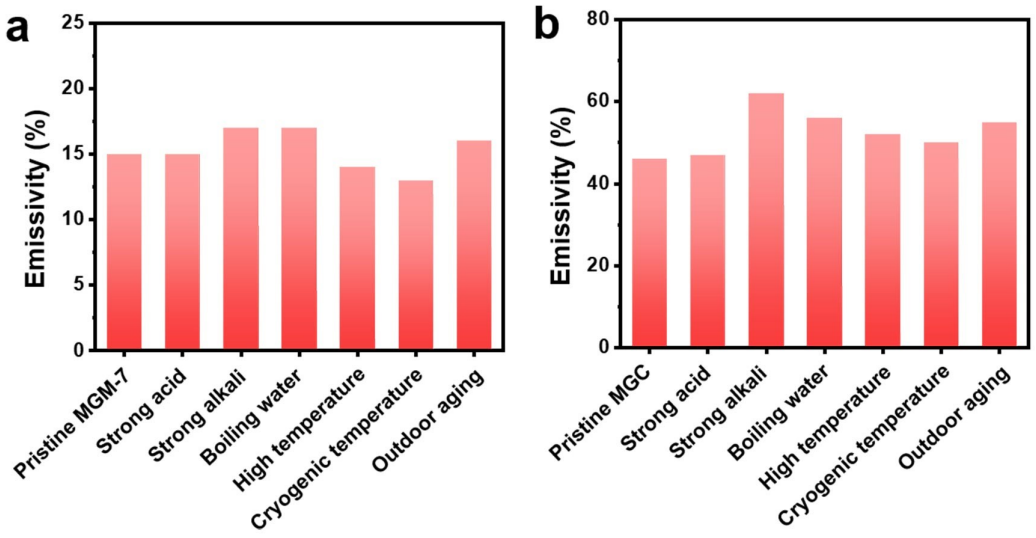

Fig. S30 IR emissivity of (a) MGM-7 films and (b) MGC films after resisting various scenarios. The IR emissivity here was measured using a radiation compensation method. Based on the Stefan–Boltzmann law: $P = \varepsilon\sigma T^4$ (σ is the Stefan–Boltzmann constant), the thermal radiation of an object is directly determined by the surface IR emissivity (ε) and the fourth power of the surface thermodynamic temperature (T). In brief, the radiation compensation method is to change the radiation temperature of an object by adjusting the emissivity of the IR camera. The emissivity of the IR camera is just the emissivity of the observed object when the radiation temperature is the same as the surface temperature measured by the thermocouple. The IR emissivity obtained using the radiation compensation method is an average value.

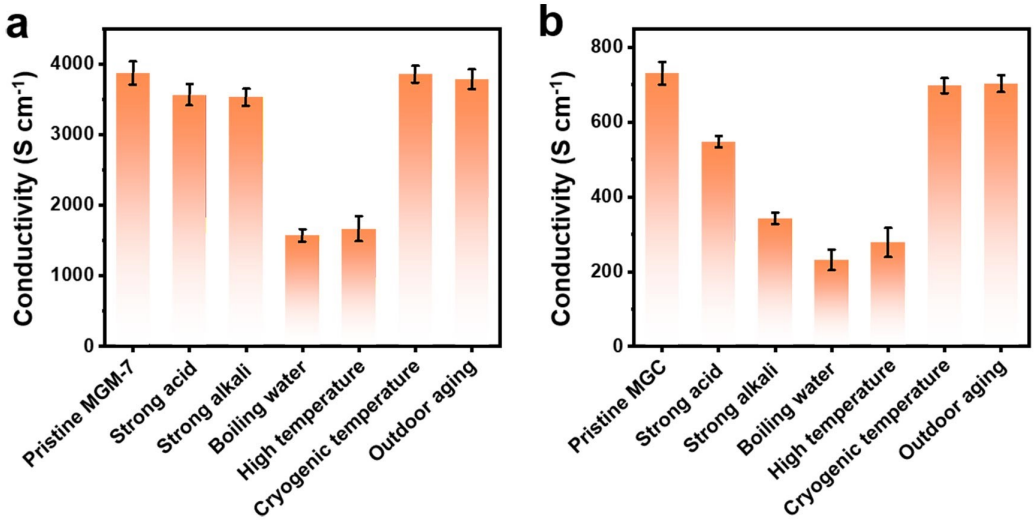

Fig. S31 Electrical conductivity of (a) MGM-7 films and (b) MGC films after resisting various scenarios.

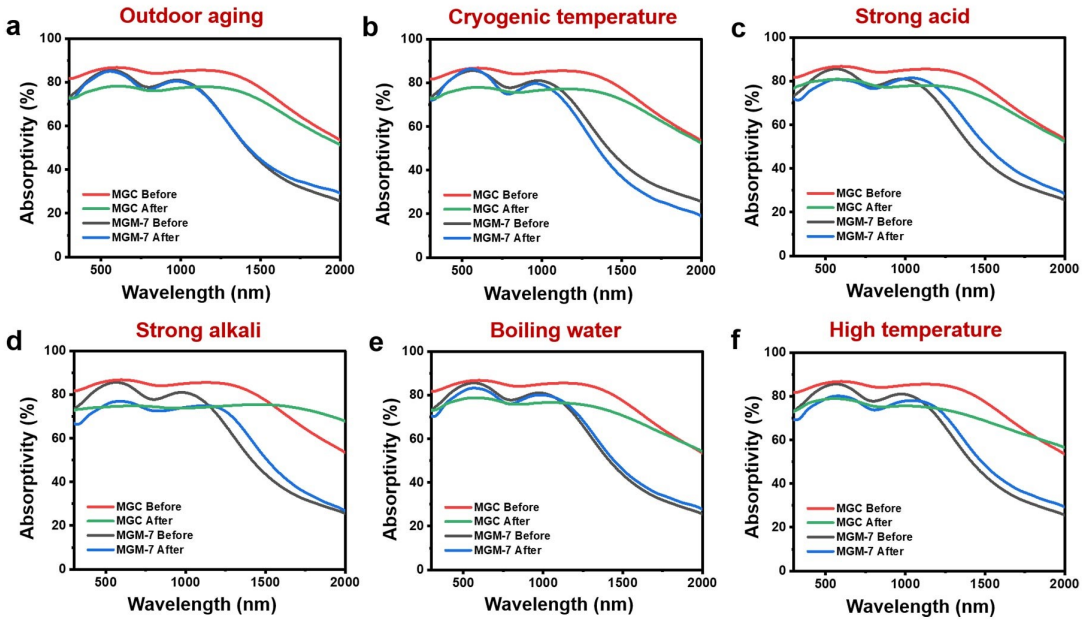

Fig. S32 Measured absorptivity of MGM-7 films and MGC films from ultraviolet to near-infrared wavelength before and after resisting various scenarios. (a) outdoor aging, (b) cryogenic temperature, (c) strong acid, (d) strong alkali, (e) boiling water, and (f) high temperature.

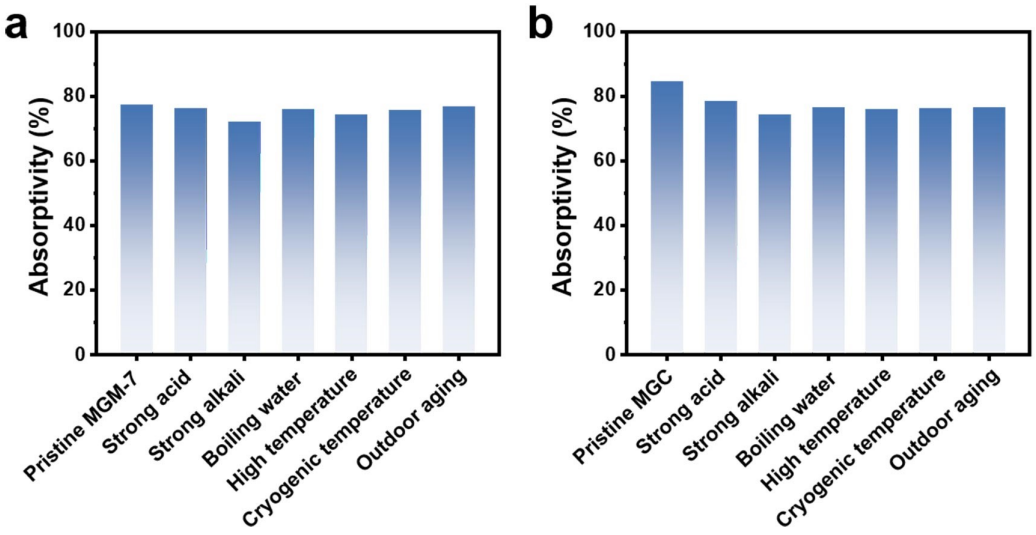

Fig. S33 Solar absorptivity of (a) MGM-7 films and (b) MGC films after resisting various scenarios.

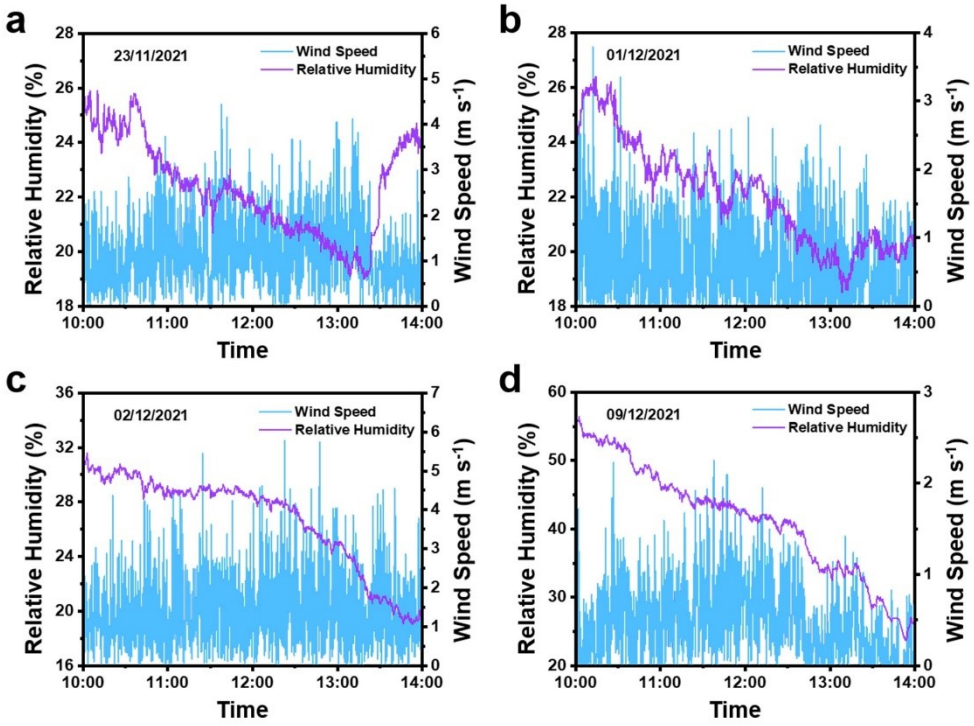

Fig. S34 Wind speed and relative humidity from 10:00 to 14:00 on (a) November 23, (b) December 01, (c) December 02, and (d) December 09 (2021, east longitude: 113°32′; northern latitude: 34°48′).

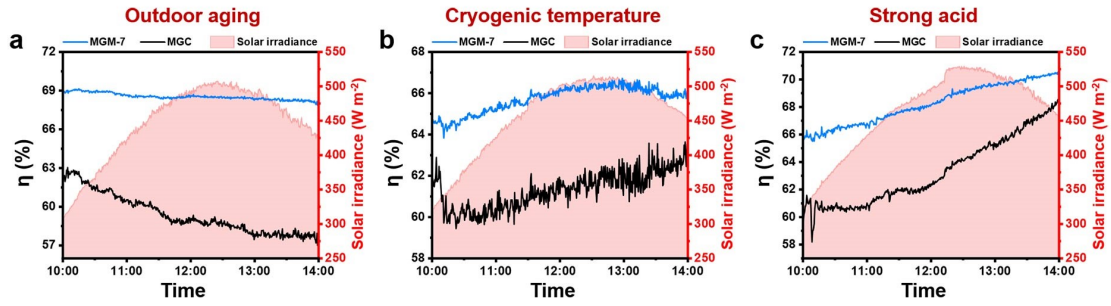

Fig. S35 Solar-to-thermal conversion efficiency of MGM-7 films and MGC films after resisting (a) outdoor aging, (b) cryogenic temperature (−196 °C), and (c) strong acid.

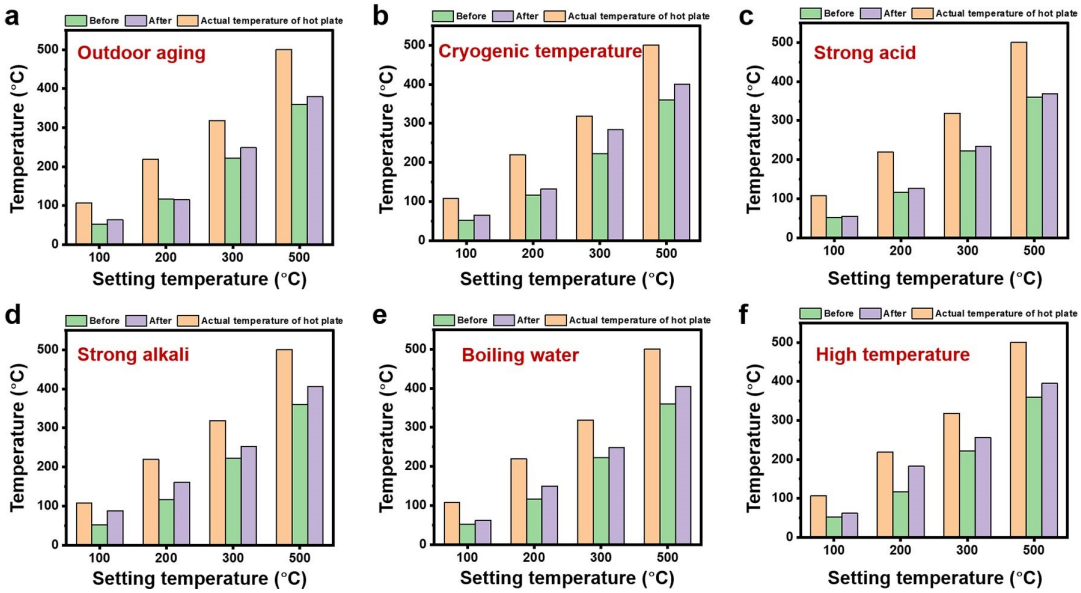

Fig. S36 IR thermal camouflage temperature changes of MGC films before and after resisting various scenarios. (a) outdoor aging, (b) cryogenic temperature, (c) strong acid, (d) strong alkali, (e) boiling water, and (f) high temperature.

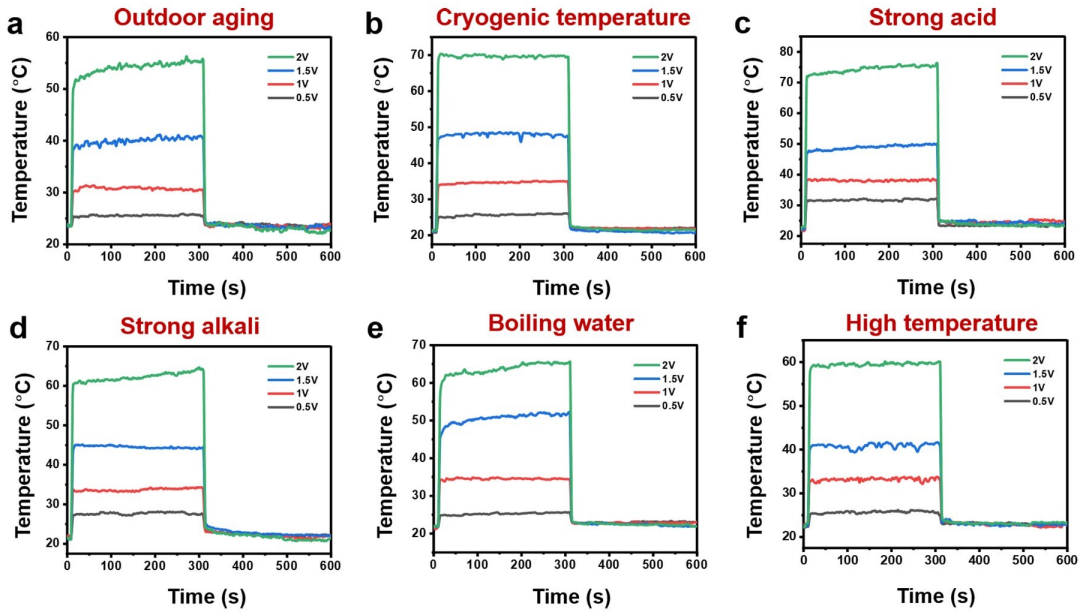

Fig. S37 Actual temperature of MGC films at different driving voltages after resisting various scenarios. (a) outdoor aging, (b) cryogenic temperature, (c) strong acid, (d) strong alkali, (e) boiling water, and (f) high temperature.

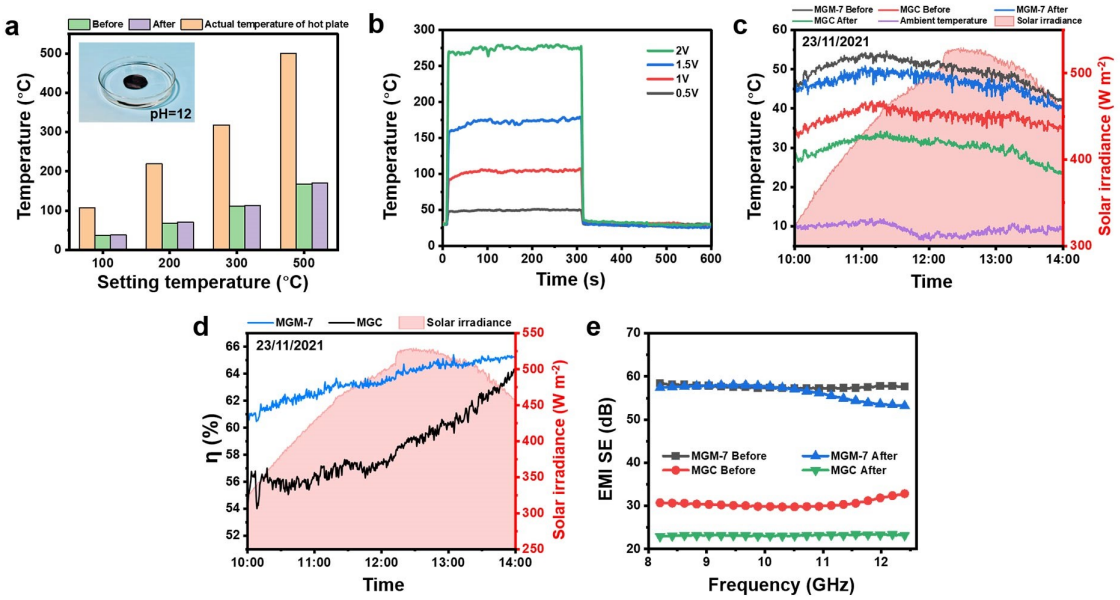

Fig. S38 Functional performances of MGM-7 films after being immersed in strong alkali: (a) IR thermal camouflage temperature changes, (b) real-time temperature and (c) solar-to-thermal conversion efficiency of strong alkali treated films on a sunny day from 10:00 to 14:00 (November 23, 2021), (d) actual temperature of strong alkali treated MGM-7 film at different driving voltages, (e) EMI SE. After being immersed in strong alkali for 2 hours, the MGM-7 film exhibits stable functional performances: a remarkable thermal camouflage performance with a highest radiation temperature reduction of 329 ℃; a saturated Joule heating temperature of 280 ℃ at 2 V; a maximum solar heating temperature of 50.9 ℃ with a solar-to-thermal conversion efficiency of 63.5% under practical solar irradiation (464 W m^{-2}); an EMI SE of 56.4 dB.

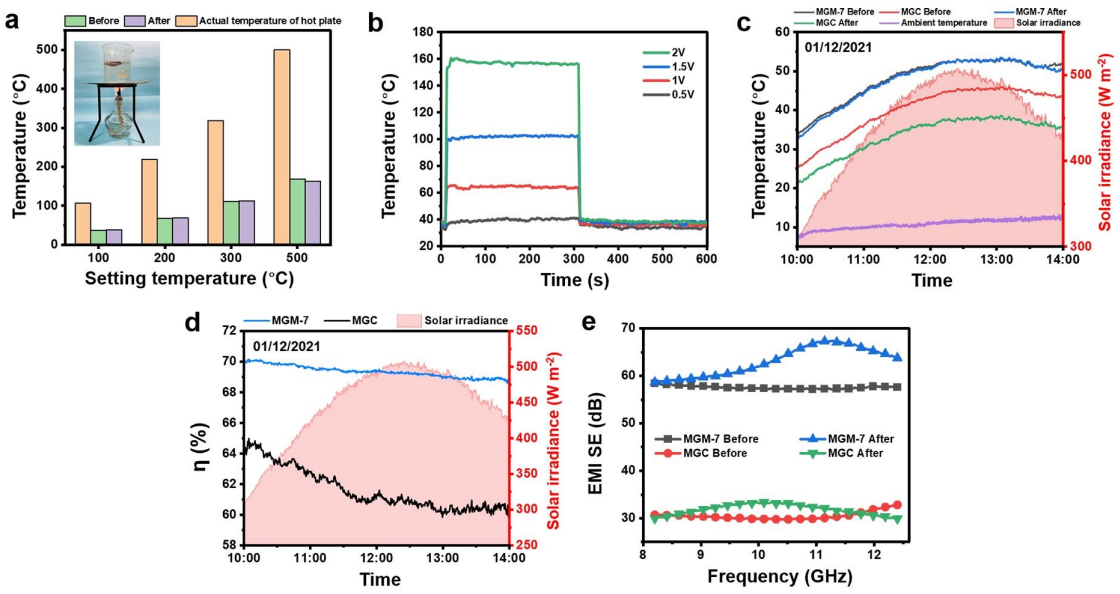

Fig. S39 Functional performances of MGM-7 films after being immersed in boiling water: (a) IR thermal camouflage temperature changes. (b) real-time temperature and (c) solar-to-thermal conversion efficiency of boiling water treated films on a sunny day from 10:00 to 14:00 (December 01, 2021), (d) actual temperature of boiling water treated MGM-7 film, (e) EMI SE. After being immersed in boiling water for 5 mins, the MGM-7 film exhibits stable functional performances: a remarkable thermal camouflage performance with a highest radiation temperature reduction of 338 ℃; a saturated Joule heating temperature of 160 ℃ at 2 V; a maximum solar heating temperature of 53.5 ℃ with a solar-to-thermal conversion efficiency of 69.4% under practical solar irradiation (447 W m^{-2}); an EMI SE of 63.1 dB.

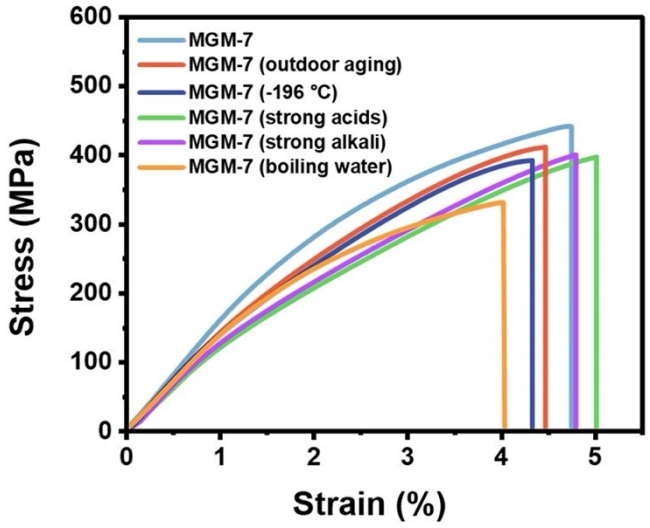

Fig. S40 Mechanical properties of MGM-7 films after utilization in various scenarios.

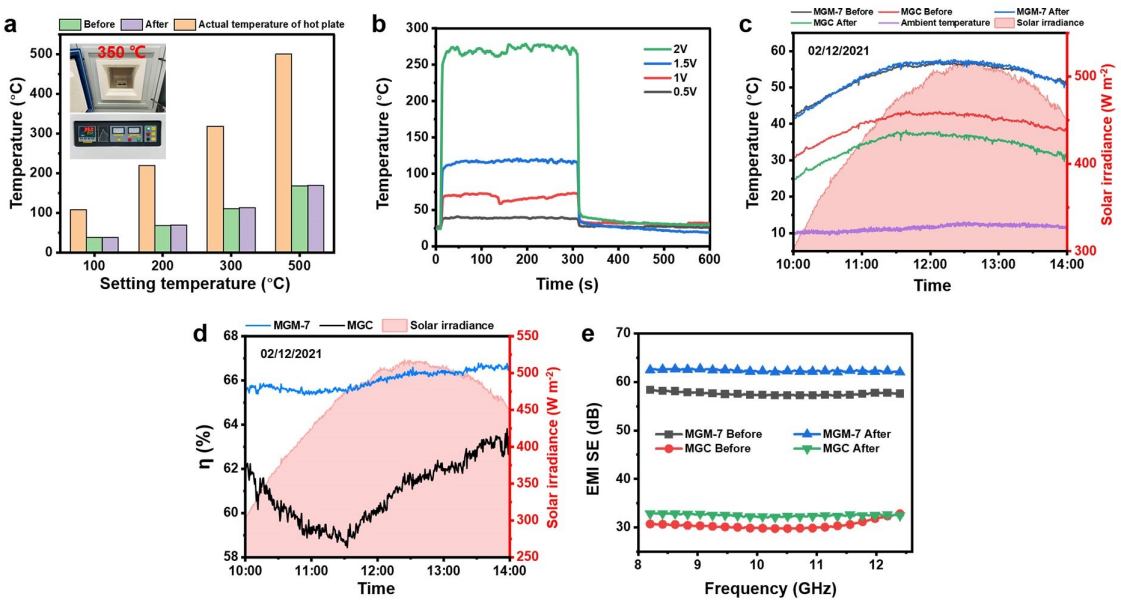

Fig. S41 Functional performances of MGM-7 films after being resisting high temperature (350 °C): (a) IR thermal camouflage temperature changes, (b) real-time temperature and (c) solar-to-thermal conversion efficiency of outdoor-aging treated films on a sunny day from 10:00 to 14:00 (December 02, 2021), (d) actual temperature of outdoor-aging treated MGM-7 films, (e) EMI SE. After high temperature aging, the MGM-7 film exhibits stable functional performances: a remarkable thermal camouflage performance with a highest radiation temperature reduction of 331 ℃; a saturated Joule heating temperature of 278 ℃ at 2 V; a maximum solar heating temperature of 57.6 ℃ with a solar-to-thermal conversion efficiency of 66% under practical solar irradiation (458 W m^{-2}); an EMI SE of 62.3 dB.

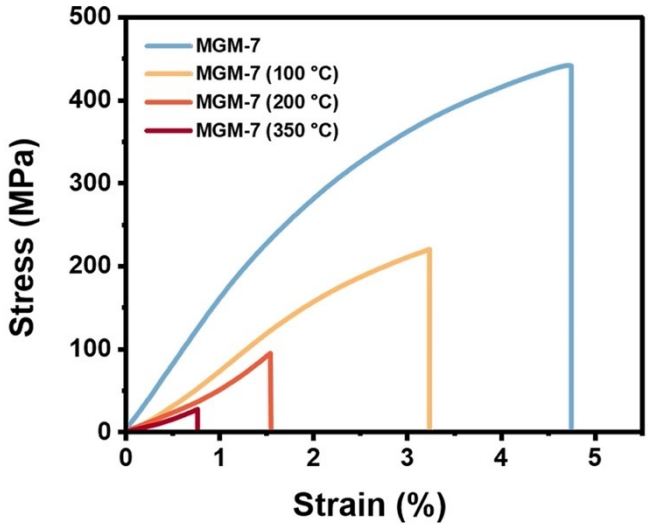

Fig. S42 Mechanical properties of MGM-7 films after aging at different high temperatures.

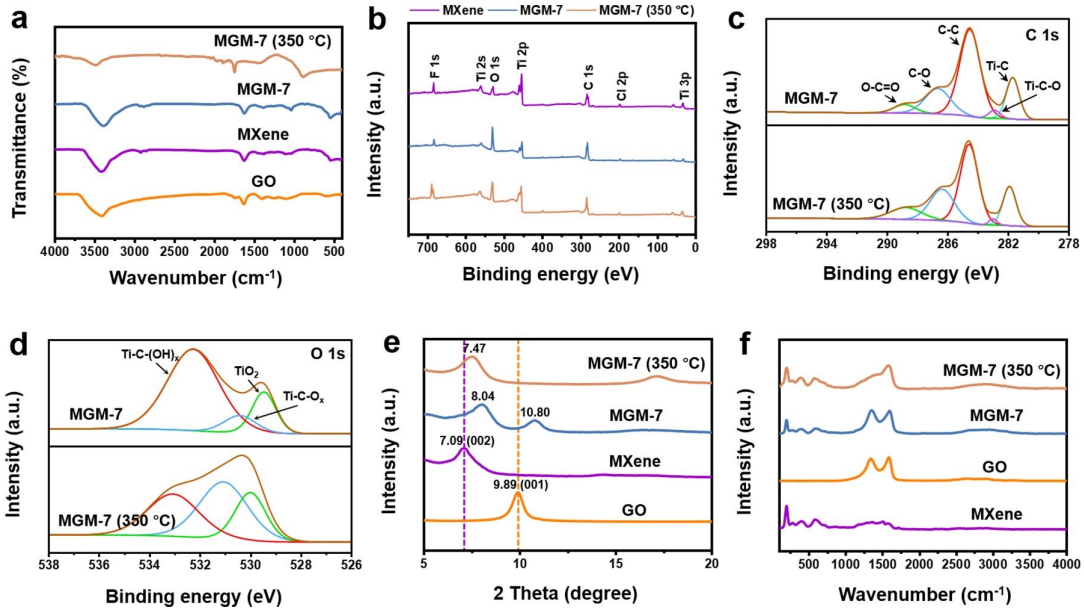

Fig. S43 (a) FTIR spectra of GO, MXene, MGM-7, and MGM-7 (350 ℃) films. (b) XPS wide-scan spectra of MXene, MGM-7 and MGM-7 (350 ℃) films. High-resolution XPS spectra of (c) C 1s and (d) O 1s for MGM-7 and MGM-7 (350 ℃) films. (e) XRD patterns and (f) Raman spectra of MXene, GO, MGM-7 and MGM-7 (350 ℃) films.

It can be clearly found from Fig. S43a that after high-temperature aging at 350 ℃, the stretching vibration peak of -OH for MGM (350 ℃) film blue-shifted significantly and the intensity of the peak was weakened severely. This indicates that after high-temperature aging, large number of hydrogen bonds in MGM film were broken. The results from Fig. S43b, S43c and S43d show that all MXene peaks were detected in MGM (350 ℃) film (Fig. S43b), indicating that the structure of MXene nanosheets in MGM (350 ℃) film were not seriously damaged during high-temperature aging process. The C 1s spectrum (Fig. S43c) shows that the peaks of C-O at 286.8 eV and C=O at 289.1 eV in MGM film shifted to lower binding energies (i.e., 286.4 and 288.8 eV) in MGM (350 ℃) film. Moreover, both peaks were stronger in MGM (350 ℃) film than those in MGM film, which is attributed to the occurred oxidation during high-temperature aging process. In the O 1s spectrum of XPS (Fig. S43d), the characteristic peak of TiO_2 in MGM (350 ℃) film shifted from 529.5 eV in MGM film to a higher binding energy of 530.0 eV, and the intensity also increased. This indicates that MGM (350 ℃) film produced more TiO_2 internally after high-temperature aging. XRD results in Fig. S43e shows that the (002) reflection at 8.04° observed in MGM film shifted to 7.47° in MGM (350 ℃) film due to the presence of TiO_2 crystals. As expected, MXene crystal structure in MGM (350 ℃) films were not severely altered even after high-temperature aging. The (001) characteristic peak of GO nanosheets, however, was disappeared in MGM (350 ℃) film, indicating that GO component suffered severe oxidation under high temperature. In Raman spectroscopy results shown in Fig. S43f, we also observed the characteristic fingerprint region of MXene in MGM

(350 °C) film. This further demonstrates that MXene component in MGM film maintained its chemical structure even after high-temperature aging. However, it is clearly that the acoustic vibration peak D induced by the GO lattice disorder was significantly weakened after high-temperature aging and shows graphitization, which again proves that GO component has been severely damaged.

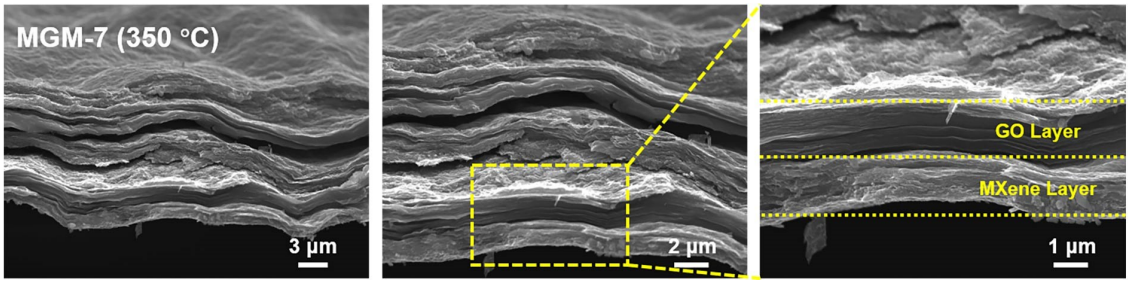

Fig. S44 Cross-sectional SEM images of MGM-7 after aging at 350 °C film at different magnifications.

One can observe that the internal structure of MGM film after high temperature aging suffered more serious damage due to the oxidation of MXene and GO components, and it was difficult to clearly distinguish the layer structure. In addition, a significant delamination occurred inside the MGM (350 °C) film due to large number of hydrogen bonds break under high-temperature. Excitingly, the MXene layer located on the surface of the film still maintains a relatively dense layer structure. Combined with the above chemical structure analysis, delaminated internal structure and severe oxidation of the mechanically reinforced GO layer are the main reasons for the drastic degradation of the mechanical properties of the MGM (350 °C) films. However, the high temperature did not cause serious damage to the functionality of

MXene layer. This is the reason why MGM (350 °C) films could maintain relatively stable electrical properties, IR thermal camouflage, Joule/solar heating and electromagnetic shielding.

Table S1. Comparison of mechanical properties of different film materials.

Materials	Density [g/cm^3]	Emissivity [100%]	Strength [MPa]	Specific strength [kN·m/kg]
Ag	10.15	0.064	134.2	13.2
Cu	7.79	0.106	204.8	26.3
Al	3.11	0.083	112	36
Stainless steel	6.78	0.155	415	61.2
Graphene	2.01	0.353	177.2	88
GO	1.89	0.667	146.4	77.3
SWCNT	0.83	0.16	150.9	181.6
PTFE	2.15	0.9	152.4	70.8
PET	1.35	0.918	122.1	90.6
PI	1.4	0.703	193.2	138
MGC	1.83	0.46	278	152.2
MXene	1.65	0.09	44.8	27.2
MGM-7	**2.30**	**0.12**	**422**	**184**

Table S2. Comparison of thermal camouflage performance of different composite materials. The references in this table correspond to those in the manuscript.

Materials	Thickness [μm]	Object temperature [°C]	Radiation temperature [°C]	Temperature reduction [°C]	Emissivity [100%]	Ref.
Ge/ZnS	9	300	77	223	0.078	49
WVO_2	200.09	65	10	55	0.35	2
Au/ZnS/Au	0.6	100	35	65	0.14	8
Pt-Ag	1000	50	28.9	21.1	0.62	9
Si-GST-Au	1	74	32	42	0.33	50
rGO-SSA	1000.15	300	25	275	0.04	51
Ag/Ge Multilayer film	1	135	77.3	57.7	0.31	52
KNA-KNA/PEG	250	60	35	25	0.94	53
Multilayer-Graphene	50	55	30	25	0.32	54
VO_2 nanopowders	1000	90	60	30	0.36	55
Leather-SiO_2	300	72	20	52	0.63	56
MZT	2100	70	15.7	54.3	/	57
PLA/TPU/GO	3000	70	52.8	17.3	/	58
PPTA/PEG	2000	50	25	25	/	59
MXene film	13	510.9	212	298.9	/	19
MXene film	29	510.9	196.4	314.5	0.19	19
MXene film	45	510.9	181	319.9	/	19
MXene film	7	511	168	343	0.09	This work
MGM-7 film	**7**	**511**	**176**	**335**	**0.12**	**This work**

Table S3. Comparison of heating performance of the recently reported different materials. The references in this table correspond to those in the manuscript.

Materials	Sheet resistance [Ω sq^{-1}]	Voltage [V]	Temperature [°C]	Ref.
CuZr Metallic glasses/ PDMS	4	7	180	29
AgNW/PVA	26	5	74	60
AgNW/Alumina	15	6	98	30
CuNi MESH/PES	/	6	150	61
Graphene	/	3.2	42	62
Liquid-metal/PDMS	/	3.5	95.9	63
CNT/TPU	/	6	65	64
AgNW/SWCNT/PDMS	/	5	87	65
AgNW/Aramid Nanofibers	3.2	5	103.5	66
CNT/FC/Aramid Nanofiber	/	10	113.5	67
MWCNT	699	15	77	68
CuNW/PE Microfibers	2.5	3	57	69
CNT Fiber	/	5	135	70
PEDOT/Cotton	61	6	45	71
MXene-PPy/PET	/	4	79	72
Conductive Weft-knitted Fabric	1.89	3.5	140	73
CNT Fiber	/	1.5	47	74
Silica NP/PDMS/AgNW/Cotton	2.8~4	0.5	34.1	75
Ag/$Ni_{0.33}Co_{0.67}$ Se/PDMS/rGO/Woven Kevlar Fiber	/	2.1	79	76
MXene film	/	2	410	This work
MGM-7 film	**/**	**2**	**350**	**This work**

Table S4. Comparison of EMI SE_t versus tensile strength of different composite materials. The references in this table correspond to those in the manuscript.

Materials	Thickness [μm]	Content [wt%]	Strength [MPa]	SEt [dB cm^{-1}]	Ref.
MXene/CNF	16.7	50	135.4	14970	29
MXene/PEDOTPSS	11	87.5	13.7	38272	77
MXene/GO	7	50	209	41428	30
MXene/TOCNF	47	50	141.9	6957	78
CNF@MXene	35	50	112.5	11314	48
MXene/ANF	23	50	83.9	10434	79
rGO/CNF	23	50	67.7	11391	80
$Ti_3C_2T_x$/BCs	5.2	55.8	176.9	49423	35
$Ti_3C_2T_x$/CNTs/CNF	38	73	97.9	10105	81
$Ti_3C_2T_x$/BCs	4	76.9	112.5	92500	35
CNT/Epoxy	2000	0.66	79.2	165	82
rGO/Fe_3O_4/PVC	1800	10	21.5	72	83
$Ti_3C_2T_x$/Xanthan	6.84	33	116.48	49854	84
AgNW/PANI	13	14	44	38461	85
CNT/NR	250	50	22.2	1788	86
GNS/NFC	13	90	61	33077	87
$Ti_3C_2T_x$/dopamine	8.85	10	309.8	78908	28
PVDF/CNT/Co	400	12	70	1142	88
Graphene film	10	100	128	43800	89
ANF/MXene/AgNWs	45	50	235.9	10689	36
rGO/MXene	60	10	24.5	4516.67	90
GO/MXene	7	90	64	71671	30
MXene/NR	251	6.71	18.25	2135.5	91
MXene/Fe_3O_4/PVA	80	/	27.7	5000	92

MXene/PNFs	28	90	65.7	15412.2	93
MXene film	7	100	44.8	51000	This work
MGC film	7	50	278	43857	This work
MGM-7 film	**7**	**50**	**422**	**83429**	**This work**

Table S5. Comparison on the EMI shielding performance of various MXene-based films taking EMI SE, SE_t, SSE_t, thickness, content, and strength into consideration at the same time. The references in this table correspond to those in the manuscript.

Materials	Strength [MPa]	SE [dB]	Thickness [μm]	Content [wt%]	SSE_t [dB cm^2 g^{-1}]	SE_t [dB cm^{-1}]	Ref.
MXene/CNF	135.4	25	16.7	50	1326	14970	29
MXene/PEDOTPSS	13.7	42.1	11	87.5	19497	38272	77
$Ti_3C_2T_x$/BCs	176.9	26	5.2	55.8	22857	50000	35
MXene/TONCF	141.9	32.7	47	50	4761	6957	78
CNF@MXene	112.5	39.6	35	50	7029	11314	48
ANF-MXene@AgNWs	181.6	57.3	50	40	9317	11460	36
rGO/MXene	24.5	27.1	60	10	29106	4516.67	90
MXene/PNFs	65.7	43	28	90	8399	15412.2	93
MXene film	44.8	35.7	7	100	30909	51000	This work
MGM-7 film	**422**	**58.4**	**7**	**50**	**36273**	**83429**	**This work**